European Journal of Mechanics / A Solids 81 (2020) 103966

Contents lists available at ScienceDirect

European Journal of Mechanics / A Solids

journal homepage: www.elsevier.com/locate/ejmsol

Testing and simulation of additively manufactured AlSi10Mg components under quasi-static loading

Miguel Costas [a,*], David Morin [a], Mario de Lucio [b], Magnus Langseth [a]

[a] Structural Impact Laboratory (SIMLab) and Centre for Advanced Structural Analysis (CASA), Department of Structural Engineering, Norwegian University of Science and Technology (NTNU), NO-7491 Trondheim, Norway

[b] Structural Mechanics Group, School of Civil Engineering, Universidade da Coruña, Campus de Elviña, 15071, A Coruña, Spain

ARTICLE INFO

Keywords:
Additive manufacturing
AlSi10Mg
3D-printed aluminium
Lateral crushing
Finite elements

ABSTRACT

An experimental and numerical study on the quasi-static loading of AlSi10Mg square boxes produced by selective laser melting (SLM) was carried out. The goal was to evaluate the applicability of common finite element modelling techniques to 3D-printed parts at material and component scales, under large deformations and fracture. Uniaxial tensile specimens were extracted and tested at different orientations, and a hypo-elastic–plastic model with Voce hardening and Cockcroft–Latham's fracture criterion was calibrated against the experimental results. The boxes were crushed laterally until failure using a spherical actuator. The considered material and finite element models were proved well suited for the prediction of the structural response of the additively manufactured components in the studied scenario.

1. Introduction

Metal additive manufacturing has experienced an exponential development in the last few years. The idea of producing complex parts without the limitations or constraints inherent to traditional manufacturing routes makes the technology very attractive for a wide range of applications like medicine, engineering, architecture, or art and design. In the field of engineering, and even though the technology is still too expensive to incorporate into mass production, additive manufacturing is already of great interest for the offshore and spacecraft industries and agencies, where shipping spare parts or tools for maintenance gives rise to greater difficulties. The development of the additive manufacturing technology entails the need for specific studies characterising the manufactured products from a wide variety of points of view, ranging from micromechanical properties (Andani et al., 2018) to lifecycle management (Müller et al., 2018).

Among all the metal powders available nowadays for additive manufacturing, Al–Si–Mg alloys manufactured by Selective Laser Melting (SLM) are some of the most popular due to their good mechanical properties and low density (Trevisan et al., 2017). SLM consists of a sequential application of powdered material in layers, which are welded together by means of a laser beam. This technology enables the manufacturing of robust and well bonded metal parts (Kruth et al., 2005, 2007).

Given the good mechanical properties exhibited by SLM-manufactured Al–Si–Mg alloys, it is not surprising that the number of dedicated investigations has rapidly increased during the last years, most of them focusing on understanding the particular microstructure of the printed alloy and how it relates to the macroscopic mechanical properties. In this vein, Larrosa et al. (2018) carried out a comprehensive study on the microstructure and processing defects of AlSi10Mg samples fabricated by SLM, linking them to the plasticity and fatigue performance of the metal. This study also compared as-printed samples which were heat-treated to peak strength (T6) or post-processed by hot isostatic pressing (HIP). Heat-treatment of additively manufactured AlSi10Mg parts was also studied in Girelli et al. (2019a), Zhou et al. (2018), where the microstructure of the treated samples was compared with a similar cast alloy subjected to the same heat treatment. Just like aluminium alloys manufactured by traditional routes, crystal plasticity models have been applied to AlSi10Mg parts produced by SLM in Kim et al. (2017), with the aim of shedding some light on the stress–strain relationship between the constituents of the alloy. One last remarkable fact on the relation between micro- and macroscopic mechanical properties can be found in the study of the boundaries of the melt pools generated by the laser in each pass (Xiong et al., 2019). This study suggested that the anisotropy of the AlSi10Mg produced by SLM and the way cracks propagate are governed by the properties of the melt pool boundaries. It is worth mentioning that a commonly reported fact in most of the

* Corresponding author.
E-mail addresses: miguel.costas@ntnu.no (M. Costas), david.morin@ntnu.no (D. Morin), m.delucio@udc.es (M. de Lucio), magnus.langseth@ntnu.no (M. Langseth).

https://doi.org/10.1016/j.euromechsol.2020.103966
Received 19 August 2019; Received in revised form 28 January 2020; Accepted 7 February 2020
Available online 11 February 2020

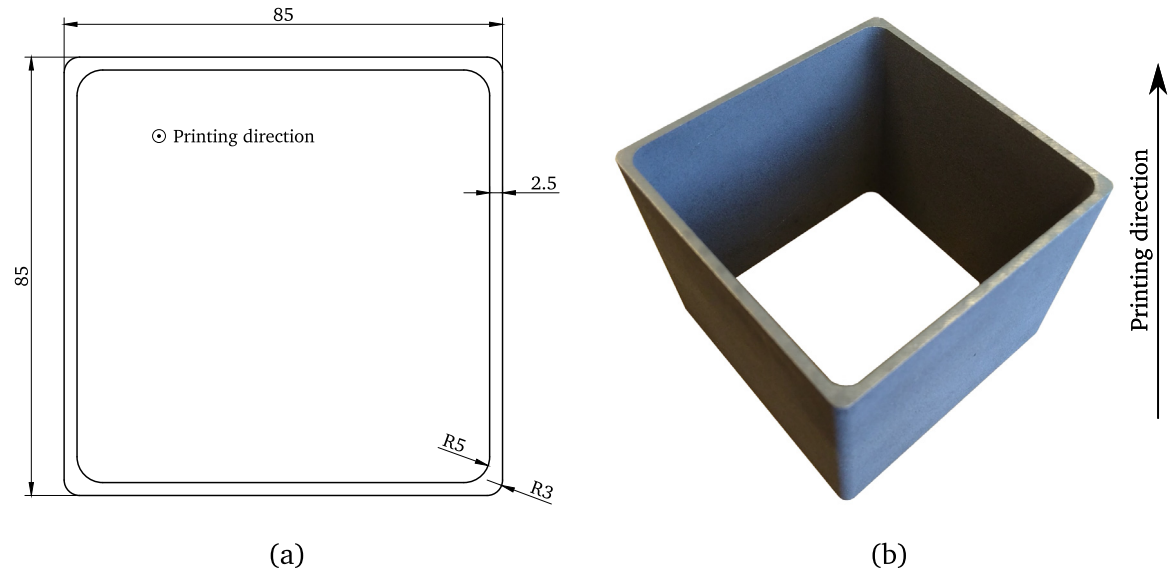

Fig. 1. Description of the manufactured components: nominal dimensions in mm (a) and picture of one of the components (b). The boxes had a height of 70 mm.

previous studies is the elevated porosity of the additively manufactured AlSi10Mg (Tang and Pistorius, 2017; Weingarten et al., 2015), which seems to be linked to the process parameters. Minimising this porosity is indeed one of the current main challenges in the production of aluminium parts by SLM (Aboulkhair et al., 2014; Yu et al., 2019).

Considerable effort has been also put in linking the microstructure of the SLM-manufactured AlSi10Mg alloy and its fatigue performance. A concise work by Domfang Ngnekou et al. (2019) studied this relation, reporting also that the anisotropy of the alloy is dependent on the process parameters. A similar problem was studied by Beevers et al. (2018), where the effect of fatigue on the microstructure, density, residual stresses, and mechanical properties was investigated.

With the rapid development of the so-called "micro-architectured materials", where the inner structure consists of a 3D-network of small-scale truss elements fabricated by additive manufacturing, some studies were carried out on the experimental response of these materials and their constitutive modelling (Bonatti and Mohr, 2019; Tancogne-Dejean et al., 2016). However, there is still a lack of scientific work on the behaviour of other kinds of printed parts or components under large deformations on macroscale. A study by Zhang et al. (2018) investigated the dynamic compression of honeycomb structures built by this technique, where damage was mainly compression-dominated. The work included simulations using experimental data as input, where the damage was controlled by a fracture strain dependent on the mesh size. A few other works can be found in the literature about 3D-printed metal parts under large deformations (Yang et al., 2017b,a), but very little or no focus has been put so far on the constitutive or finite-element modelling of structural components made of AlSi10Mg.

Therefore, it is still unclear whether the behaviour of these additively manufactured components can be modelled through commonly used material models, especially when the parts are subjected to complex loading scenarios. Thus, this paper contributes by evaluating the suitability of some accepted material and component modelling strategies for reproducing the experimental behaviour of additively manufactured parts subjected to lateral compression, emphasising the effect of different element types, yield criteria and calibration directions on the quality of the numerical results in comparison with experimental tests.

2. Components manufacturing

Five boxes with the dimensions provided in Fig. 1(a) were manufactured using selective laser melting (SLM). The components were built using an AlSi10Mg alloy with commercial name EOS M280, which is among the most popular for additively manufactured metal parts, as shown in the introduction. The technique starts with the application of a layer of powdered material on a building platform. Then a laser is applied on the powder so that it solidifies in the areas corresponding to the cross-section of the part. After the material solidifies, the building platform is lowered and a new layer of powder is applied. This process is repeated until the piece is completed (Trevisan et al., 2017). The temperature of the building plate was 35 degrees Celsius during the manufacturing of the parts.

In this case, the parts were built in the direction orthogonal to the cross section in Fig. 1(a) with a layer thickness of 0.03 mm. The laser that produced the micro welds penetrated approximately two layers down in each pass, according to the provider. The beam created melted pools of material that solidified shortly after each pass. A picture of a completed part is shown in Fig. 1(b).

A metallographic study was conducted on a sample extracted from one of the walls of a component, which was observed in three directions to evaluate the effects of the manufacturing process on the microstructure of the material. The sample was embedded in cold epoxy resin, roughed down with silicon carbide sanding belts of P600 and P1200, polished with lubricated cloths and diamond paste of 3 and 1 micrometres, and finally etched with a diluted aqueous solution of HF 0.05% to reveal the microstructure of the material.

The results of this metallographic study are provided in Fig. 2, where the images were treated with a colour filter to clearly depict the microstructure of the material. The passes of the laser can be observed in Fig. 2(a), which is seen from above (i.e. the displayed surface is orthogonal to the printing direction). The bands correspond to the fraction of material which is melted in each pass. The depth of these pools is clearly revealed by pictures taken in the two planes orthogonal to the previous, Figs. 2(b) and 2(c). They are approximately 50–70 μm deep, which is approximately two layers of the powdered material, in line with what had been reported by the manufacturer. A three-dimensional composition of the images is shown in Fig. 2(d) to help to visualise the microstructure of the material. As pointed out in previous studies (Larrosa et al., 2018), the obtained alloy exhibits a rather complex microstructure compared to wrought aluminium alloys, and also a markedly different grain distribution compared to cast alloys. The reader is referred to Kristoffersen et al. (2020) for a more detailed comparison of the microstructure of the current alloy with that of a cast-die alloy with the same chemical composition.

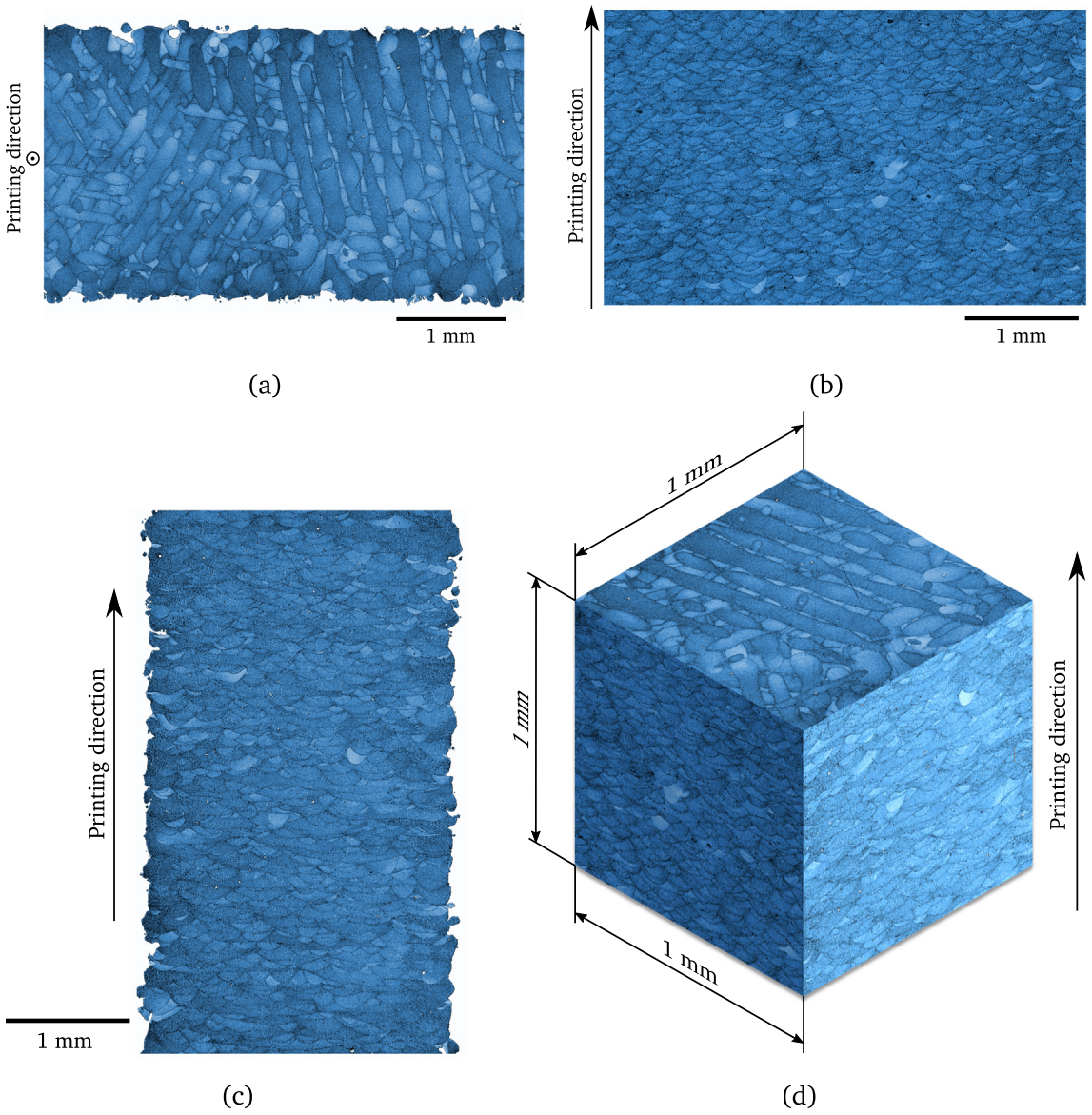

Fig. 2. Metallographic pictures of the microstructure of the as-built material: top view (a), front view (b), side view (c), and three-dimensional view (d).

3. Material tests and constitutive modelling

3.1. Uniaxial tensile tests

Tensile specimens with the dimensions shown in Fig. 3(a) were cut from one of the printed boxes using a wire electrical discharge machining (EDM) to minimise the influence of the machining on the mechanical properties. The coupons were extracted at orientations of 0, 45, and 90 degrees with respect to the printing – vertical – direction (see Fig. 3(b)).

The tensile tests were carried out at 1 mm/min in an Instron 5566 equipped with a load cell of 10 kN. Three parallel tests were run for each orientation to evaluate the repeatability and consistency of the results obtained for this alloy. The strains were computed using digital image correlation (DIC) on a series of sequential images of the specimens during the tests, whose surface was previously painted with an adequate speckle pattern. The pictures were taken with a Prosilica GC2450 digital camera at 2 frames per second with an approximate resolution of 85 pix/mm. The in-house software eCorr (Anon, 2018) was used to compute the strains. The DIC analyses were based on a 2D setup using a Q4 element formulation (Fagerholt et al., 2013). The element size in the 2D DIC mesh was 25 × 25 pixels, which approximately corresponded to 0.3 × 0.3 mm. A virtual extensometer centred in the specimen's gauge was pinned to two nodes separated 18.73 mm, providing the engineering strains.

A proper discussion on the thickness of the part and thus, of the tensile specimens, is required before computing the engineering stress–strain curves of the tests. Due to the elevated surface roughness of the printed components, which is a well known issue for AlSi10Mg and SLM (Boschetto et al., 2017; Scherillo, 2018), the determination of an effective thickness was not straightforward. The surface roughness is clearly noticeable in Figs. 2(a) and 2(c). The thickness and width of all specimens were firstly measured with a micrometre with flat heads, obtaining thicknesses between 2.612 and 2.691 mm. These measurements correspond to the maximum distance between the flat head on each side, and differ from the nominal thickness of 2.5 mm due to the elevated superficial roughness of the material. For this reason, the thickness was alternatively measured using the microscopy images. A value of 2.45 mm was obtained computing the average of the maximum and minimum distance between faces measured on the images. Thus, the engineering stress–strain curves provided in Fig. 4 were computed using the measured width of each specimen (between

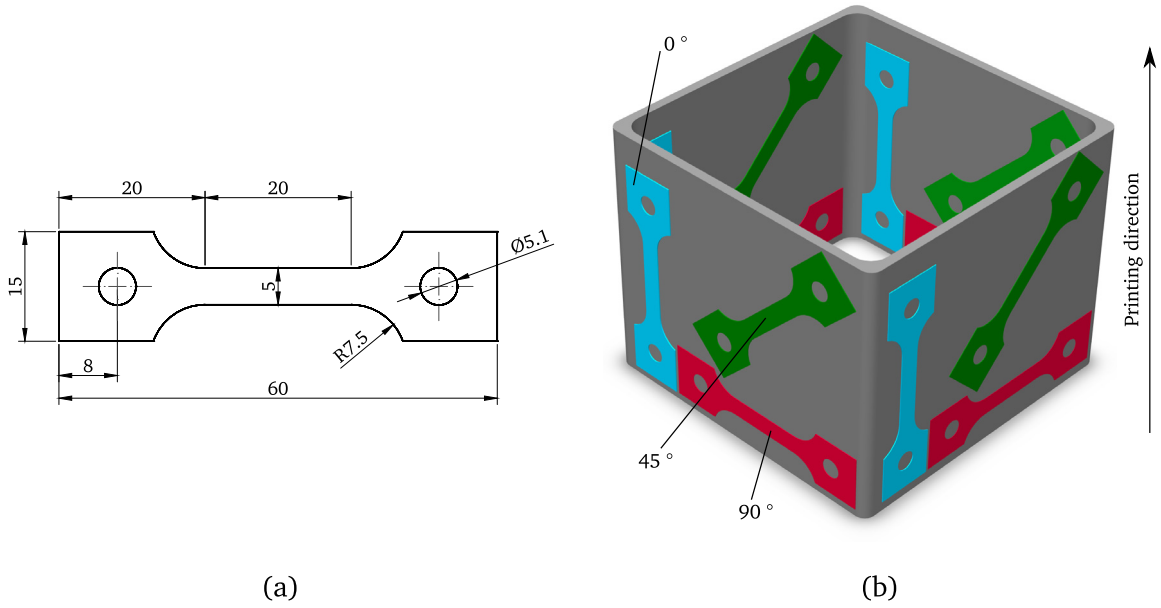

Fig. 3. Dimensions of the tensile specimens in mm (a) and extraction locations in the boxes (b).

Table 1
Engineering strain and stress at fracture measured in the tensile tests at the three different orientations with respect to the printing direction.

Orientation	Eng. strain at fracture	Eng. stress at fracture [MPa]
0°	0.0446	399.14
	0.0392	383.27
	0.0451	398.62
45°	0.0465	391.52
	0.0460	389.61
	0.0469	393.49
90°	0.0561	393.44
	0.0586	397.80
	0.0563	396.71

5.009 and 5.035 mm) and a uniform effective thickness of $t_{\text{eff}} = 2.45$ mm. The effect of adopting different effective thicknesses to compute the engineering stress–strain curves is further discussed in Section 4.5. According to the stress–strain curves shown in Fig. 4, the as-built material exhibits a weak anisotropy in terms of yield stresses and work-hardening. In the printing direction, the work hardening seems stronger than in the transverse direction (90 degrees) while the 45 degrees direction lies in between the two other directions. The opposite can be stated for the initial yield stress, which is higher in the transverse direction compared to the printing direction. In view of the failure strains, shown in Fig. 4 and Table 1, the alloy seems to have a quasi-brittle behaviour (Lemaitre and Desmorat, 2005) since plastic deformation does occur prior to failure while being small (engineering strains lower than 0.06 at failure). Failure occurred at low strains in all directions without any necking in the specimens. In terms of failure strains the anisotropy is more noticeable, with larger failure strains in the direction perpendicular to the printing axis. According to Fig. 4, the stress at failure is independent of specimen orientation, which combined with the anisotropic work-hardening leads to a macroscopic anisotropic failure. The engineering stresses and strains at failure measured in the tests are summarised in Table 1.

To investigate the mechanisms linked to the failure of this alloy, scanning electron microscopy (SEM) was used and the resulting failure surfaces are detailed in Fig. 5. It can be observed that there were no signs of ductile failure mechanisms since no large dimples can be observed in Figs. 5(a) and 5(c). Some voids can be observed in Fig. 5(b) with small dimples in between, but these voids could have been present

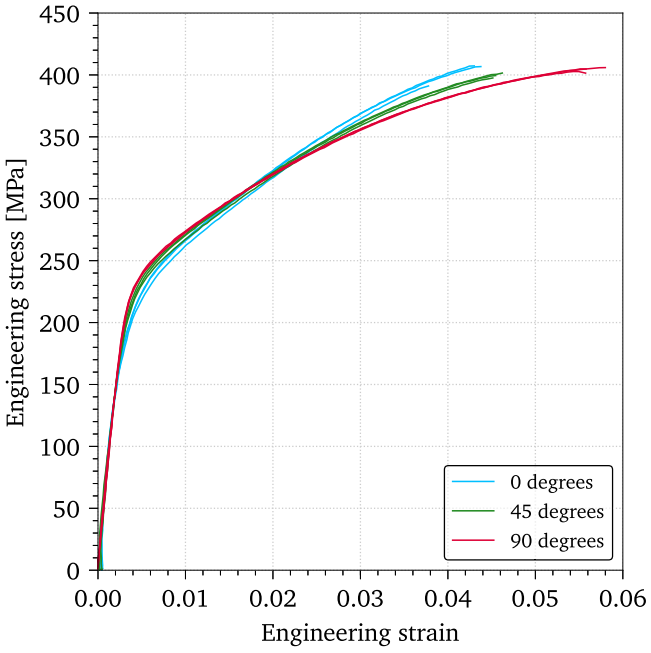

Fig. 4. Engineering stress–strain curves up to failure of the as-built AlSi10Mg at 0, 45, and 90 degrees with respect to the printing direction.

in the material before deformation. The absence of clear signs of ductile failure in the material is in line with the quasi-brittle failure shown in the stress–strain curves, Fig. 4. The morphology of the fracture surfaces provided in Fig. 5 suggests similar fracture mechanisms to those reported and investigated by other authors for the same material (Girelli et al., 2019b; Delahaye et al., 2019). Moreover, no large differences were observed between the samples at 0, 45 and 90 degrees in the SEM analyses.

Optical microscopy images of polished samples from the interior of the tensile specimens were taken before and after the tensile tests. A high density of voids can be observed already in the non-tested material (Figs. 6(a) and 6(b)), increasing somewhat towards the end of the tests (Figs. 6(c) and 6(d)). A low void growth could be expected since the

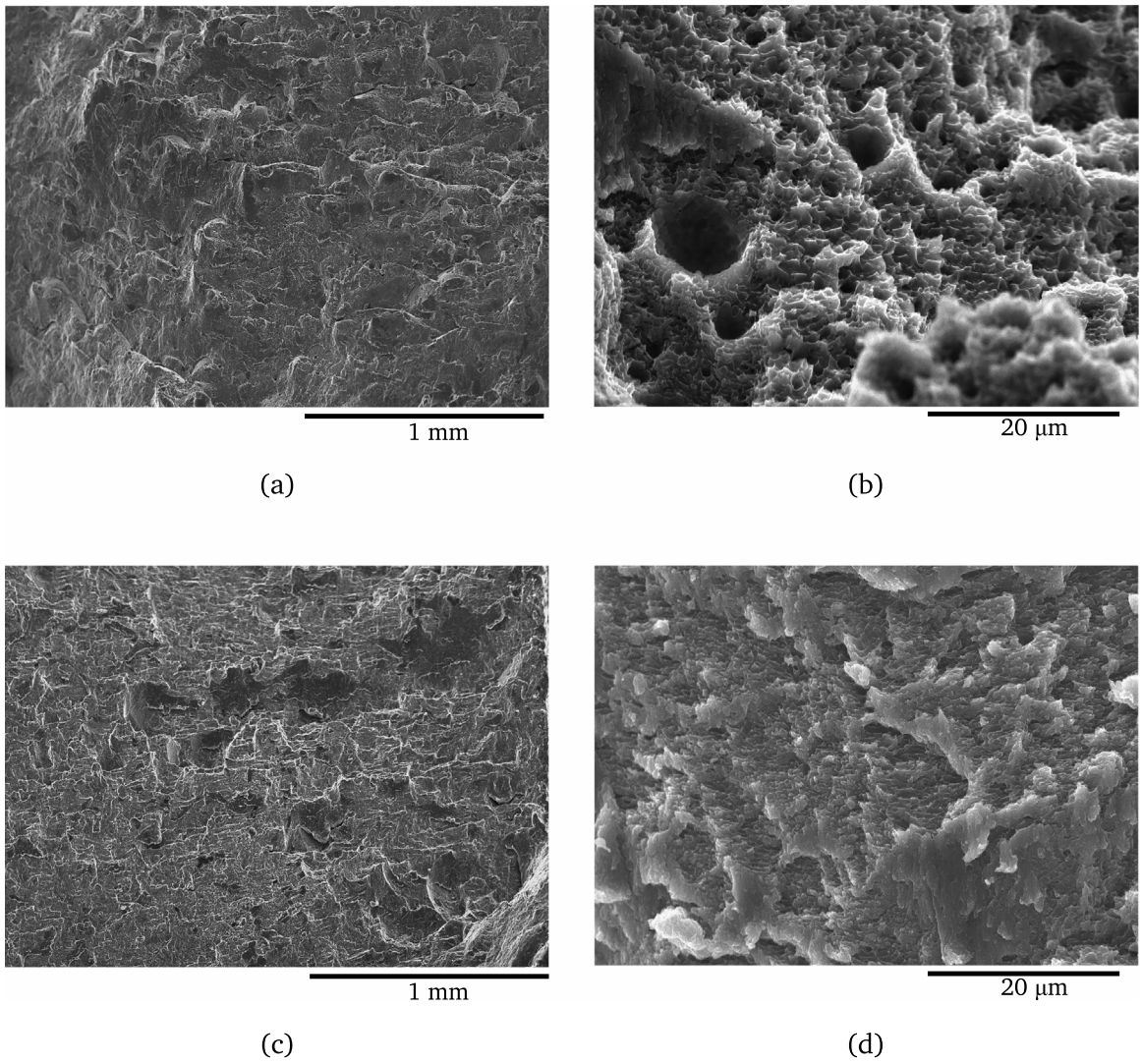

Fig. 5. SEM images of the fracture surfaces in the tensile specimens at 0 (a, b) and 90 degrees (c, d) with respect to the printing direction, under different magnification levels.

material experiences no necking. This means that the stress triaxiality remains approximately $\frac{1}{3}$ until the end of the tests.

3.2. Plastic strain ratios

The strain ratios R_θ were computed by measuring the thickness and width of the specimens before and after the tests with a micrometre, and computing the ratio of the plastic strains in the width direction to those in the thickness direction i.e.

$$R_\theta = \frac{\varepsilon^{\mathrm{p}}_{\mathrm{w},\theta}}{\varepsilon^{\mathrm{p}}_{\mathrm{t},\theta}}, \tag{1}$$

where θ is the orientation of the specimen with respect to the printing direction, and $\varepsilon^{\mathrm{p}}_{\mathrm{w}}$ and $\varepsilon^{\mathrm{p}}_{\mathrm{t}}$ are the plastic strains in the width and thickness directions, respectively. The measurements were taken at four locations in each tensile specimens. Due to small failure strains of the material and elevated superficial roughness of the component, these measurements exhibit considerable scatter. The resulting R values for the tested material in the three directions are plotted in Fig. 7. In spite of the scatter, it can be stated that the plastic strains in the width direction were smaller than those in the thickness direction, which indicates a certain strain anisotropy of the material. These results substantially differ with what is typically observed in aluminium extrusions and rolled sheets, where recrystallised or non-recrystallised microstructures lead to larger variations of the strain ratios depending on the test angle, as presented in Saai et al. (2013).

An additional study of the strain ratios between the longitudinal and width directions of the specimens was carried out using DIC measurements of the strain fields on the surfaces of the specimens' gauges. The strain ratios for these directions were computed for each tested direction θ using the following expression based on the q ratio proposed by Khadyko et al. (2017):

$$q_\theta = -\frac{\mathrm{d}\varepsilon^{\mathrm{p}}_{\mathrm{w},\theta}}{\mathrm{d}\varepsilon^{\mathrm{p}}_{\mathrm{l},\theta}}, \tag{2}$$

$\varepsilon^{\mathrm{p}}_{\mathrm{w}}$ and $\varepsilon^{\mathrm{p}}_{\mathrm{l}}$ being the plastic strains in the width and longitudinal directions, respectively. Notice that the previous expression differs from the definition in Khadyko et al. (2017) as in the present work the plastic strains are considered instead of the total strains. This method alleviates the uncertainty linked to the thickness of the specimens given that no measurements in the thickness direction are required.

The logarithmic strains in the longitudinal and width directions during the tests were obtained by averaging the results of the DIC analyses over all elements in each picture. These logarithmic strain fields in the longitudinal and width directions are shown in Fig. 8 right before fracture in one specimen at each orientation. It can be seen that the strain distribution on the surface of the specimens is more or less

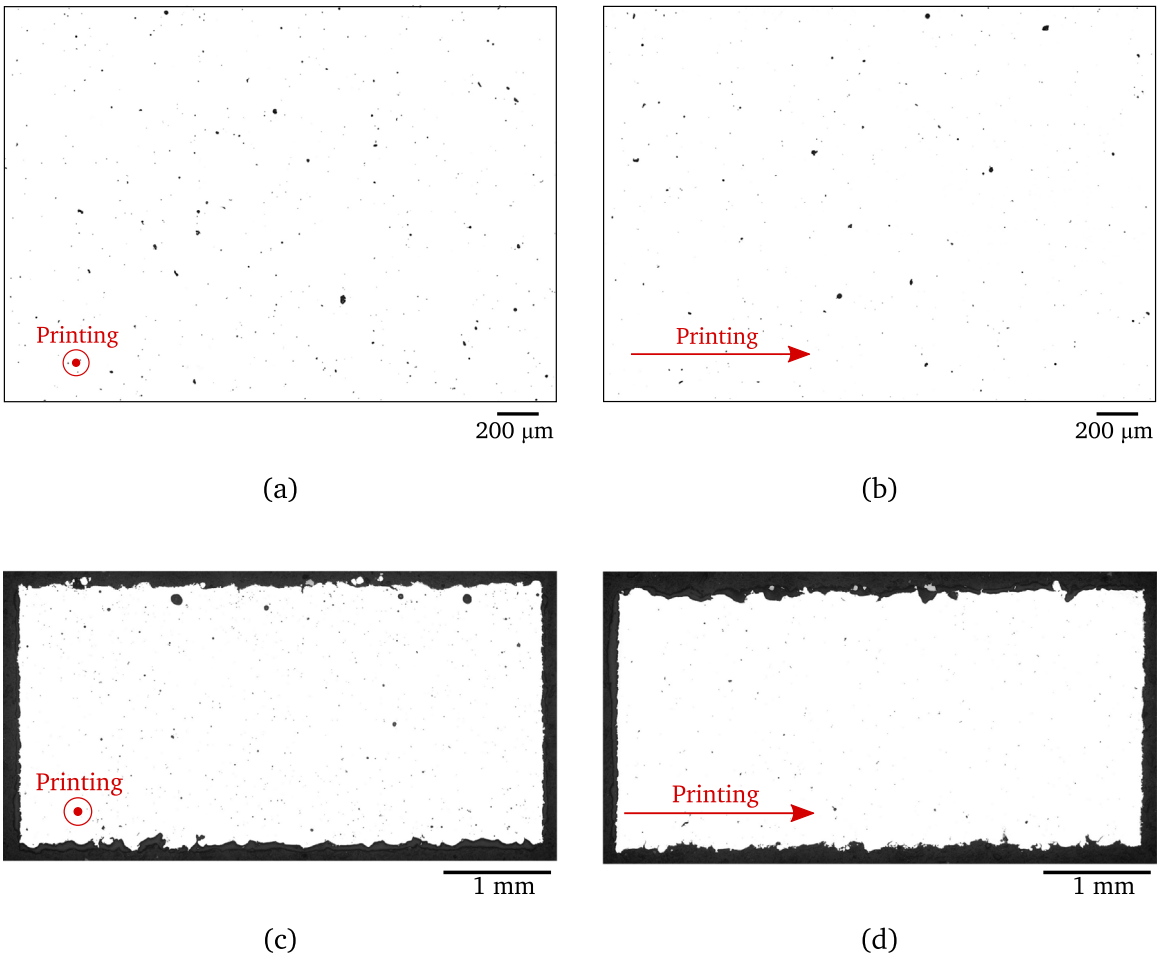

Fig. 6. Optical microscopy images of porosity in the as-built material: before tensile tests at 0 (a) and 90 (b) degrees, and gauge cross section after tensile tests at 0 (c) and 90 (d) degrees.

homogeneous at the onset of fracture, without any local necking. The elements in the DIC mesh have an approximate size of 0.3 millimetres.

The plastic strains ε_w^p and ε_l^p were obtained from the total strains measured with DIC as

$$\varepsilon_l^p = \varepsilon_l - \frac{\sigma}{E} \tag{3}$$

and

$$\varepsilon_w^p = \varepsilon_w + \nu\frac{\sigma}{E}, \tag{4}$$

where σ is the true stress, E is the elastic modulus (assumed 70 GPa), and ν is the Poisson's ratio (assumed 0.33). Fig. 9 provides the computed plastic strain paths together with a dashed line with slope −0.5, corresponding to the theoretical plastic strain path for isotropic plasticity. The averaged q values for each orientation defined according to Eq. (2) were $q_0 = 0.433$, $q_{45} = 0.374$, and $q_{90} = 0.356$.

The current results indicate a certain strain anisotropy of the as-built AlSi10Mg. This anisotropy shown by the strain ratios could be caused by the particular crystallographic texture of the alloy or the void growth in the material. However, the relatively low ductility of the material and the fact that the microscopy images do not show a remarkable growth of the voids seems to indicate that its strain anisotropy stems mainly from the former.

3.3. Constitutive modelling

Despite the observed plastic anisotropy of the material pointed out in Figs. 7 and 9, an isotropic plasticity model was adopted. Utilising a more complex yield surface suitable for this material would require further investigations. Therefore, it seems reasonable to adopt an isotropic model in a first stage to evaluate to what extent a simple model can work, given that it has been shown to provide good results with materials exhibiting strong textures (Morin et al., 2017; Costas et al., 2019). Moreover, this presents the additional advantage of being more suitable for industrial applications thanks to a simple calibration procedure.

An elastic modulus of 70 GPa and a Poisson's ratio of 0.33 were assumed for the elastic behaviour. The yield function f can be written as

$$f = \sigma_{eq} - (\sigma_0 + R) \leq 0, \tag{5}$$

where σ_{eq} is the equivalent stress, σ_0 represents the initial yield stress, and R is the isotropic hardening. Two different yield criteria were compared in the simulations, namely von Mises and Hershey–Hosford yield surfaces. The Hershey–Hosford criterion was considered here because it has been shown by Dæhli et al. (2017) to promote strain localisation and thus, reduce the ductility of aluminium alloys compared to the von Mises yield criterion. Therefore, the equivalent stress in Eq. (5) was defined in terms of the ordered principal stresses σ_1, σ_2, and σ_3 as

$$\sigma_{eq} = \sqrt{\frac{1}{2}\left[(\sigma_1 - \sigma_2)^2 + (\sigma_2 - \sigma_3)^2 + (\sigma_3 - \sigma_1)^2\right]} \tag{6}$$

for the von Mises criterion, and as

$$\sigma_{eq} = \left[\frac{1}{2}\left(|\sigma_1 - \sigma_2|^m + |\sigma_2 - \sigma_3|^m + |\sigma_3 - \sigma_1|^m\right)\right]^{\frac{1}{m}} \tag{7}$$

for the Hershey–Hosford criterion. The exponent m defines the shape of the yield surface, taken here as 8, conforming to the customary value

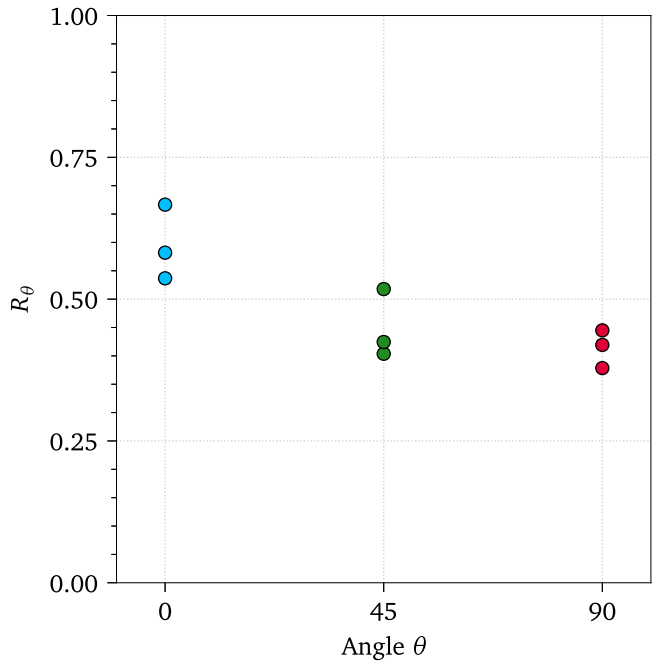

Fig. 7. Strain ratios measured in the tested tensile specimens at three different orientations θ with respect to the printing direction.

Table 2
Parameters of the extended Voce hardening rule and Cockcroft–Latham parameter for the three tested orientations and averaged RMSE, given in MPa.

Orientation	σ_0	Q_1	θ_1	Q_2	θ_2	W_c	RMSE
0° (printing)	180	39.7	45000	347	8890	12.21	3.84
45°	199	30.7	36900	296	8000	13.13	3.90
90°	213	22.6	29800	254	7690	17.22	3.71

for FCC alloys (Barlat et al., 2005). Notice here that the von Mises criterion can be seen as a particularisation of the Hershey–Hosford surface for $m = 2$ or $m = 4$. The associated flow rule was assumed in both cases.

The extended Voce hardening law with two pairs of parameters defines the work hardening R as a function of the equivalent plastic strains, reading

$$R = \sum_{i=1}^{2} Q_i \left[1 - \exp\left(-\frac{\theta_i}{Q_i} p\right)\right], \tag{8}$$

where Q_i represent the saturation stresses, θ_i are the initial hardening moduli, and p is the equivalent plastic strain. Given that the material exhibited no strain localisation, the hardening parameters were identified based on the true stress–strain curves of the experiments. Inverse modelling of the tests was also conducted, but since the tensile specimens did not reach the necking point, the results of the inverse modelling were identical to the true stress–strain fit and needed no further refinement. It is worth mentioning at this point that the hardening parameters become independent of the yield surface since the stress state remains in pure uniaxial tension until failure, and that the Hershey and von Mises yield surfaces are identical under generalised tension and compression. The Voce hardening rule was fitted to the experimental data at 0, 45 and 90 degrees with respect to the printing direction, with the aim of simply evaluating the effect of anisotropic work-hardening on the results of the simulations. This will be discussed further in Section 4.4. The parameters obtained for the three calibrations and the root-mean-square error (RMSE) averaged for the three experiments in each direction are provided in Table 2. A good fit was obtained, as shown in Fig. 10.

Failure was taken into account adopting the Cockcroft–Latham fracture criterion (Cockcroft and Latham, 1968). Despite its simplicity, this criterion has been successfully applied to a variety of problems involving material failure in complex scenarios such as large deformations of extruded profiles (Costas et al., 2019) or sandwich panels under impulsive loads (Wadley et al., 2013). This one-parameter criterion defines the damage variable D as

$$D = \int \frac{1}{W_c} \langle \sigma_1 \rangle \, \mathrm{d}p, \tag{9}$$

where W_c is an experimentally determined parameter, σ_1 is the major principal stress, $\langle \sigma_1 \rangle = \max\{\sigma_1, 0\}$, and p is the equivalent plastic strain. Failure occurs at an integration point when the damage variable equals 1. Once again, since no necking was reported in the material tests, the value of W_c becomes independent of the mesh size. The C-L parameter was computed by loading a single shell element up to experimental fracture strain and integrating the first principal stress over the equivalent plastic strain, giving the values provided in Table 2 for the three tested directions.

4. Component tests and simulations

4.1. Experimental tests

The manufactured boxes were laterally crushed until failure with a semi-spherical actuator made of high-strength steel with a diameter of 100 mm, which triggered bending around two of the component's axes. The crushing was applied at a constant velocity of 5 mm/min in an Instron 5985 testing machine, ensuring quasi-static conditions. In order to reduce the friction between the components and the machine, a Unimoly C-220 lubricant was sprayed on the surfaces in contact before every test. A pair of Prosilica GC2450 digital cameras recorded every test from two points of view, and the readings of the cross-head displacement logged by the machine were checked by tracking a target sticker attached to the actuator with an additional camera. Four repetitions were run with very similar collapse modes and force–displacement curves, as shown in Fig. 11(a). In all tests, fracture took place first at the side walls of the boxes due to bending, Fig. 11(b). The cracks propagated rather quickly resulting in a loss of bearing capacity. This is indicated with dots in Fig. 11(a). After this failure, the components were still able to carry some load due to the contact between both fragments, but a total failure took place shortly afterwards.

The fracture surfaces in the walls of the boxes were scanned under SEM (Scanning Electron Microscopy). The fracture morphology can be observed at different magnification levels in Figs. 11(c) and 11(d), where the elevated porosity of the material is clearly seen already at low magnification levels, Fig. 11(c). The fracture morphology is in line with what was observed in the SEM images of the fractured tensile specimens.

4.2. Numerical simulations

With the aim of evaluating the applicability of the constitutive model described in Section 3.3 to 3D-printed parts, finite element models of the lateral crushing tests were built and benchmarked against the experimental results. All the finite element simulations were conducted in Abaqus/Explicit in its version 2017 (Anon, 2016) using both solid and shell elements, since the former give in general an increased accuracy and the latter require much shorter computation times. The constitutive models fitted to the experimental tensile tests in Section 3.3 were included in the simulations with a user-defined material model written in a VUMAT subroutine.

As mentioned, two different models were built using linear solid and shell elements with reduced integration. For the solids model, an element size of 0.817 mm was adopted so that three elements could be placed across the thickness of the plates. Additional runs were made

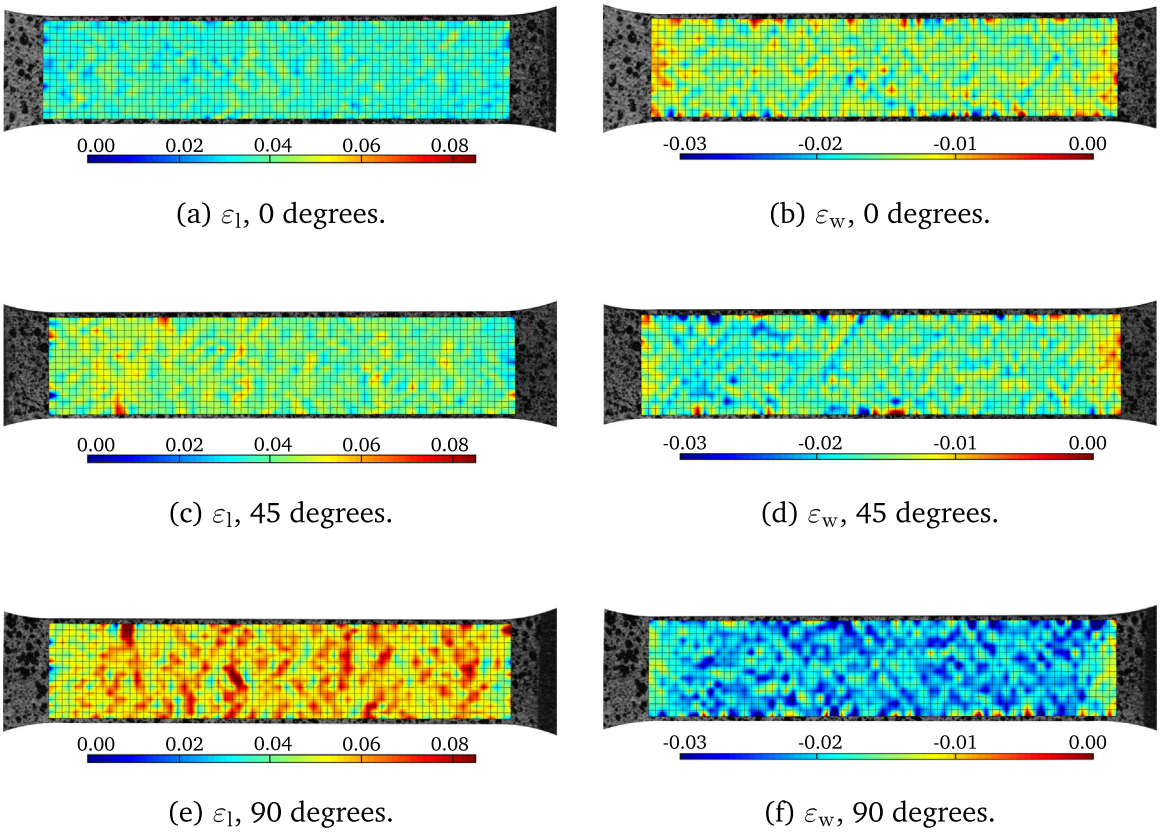

Fig. 8. Longitudinal and transverse logarithmic strain fields at the onset of fracture on the surface of the tensile specimens at 0, 45, and 90 degrees with respect to the printing direction, obtained by DIC.

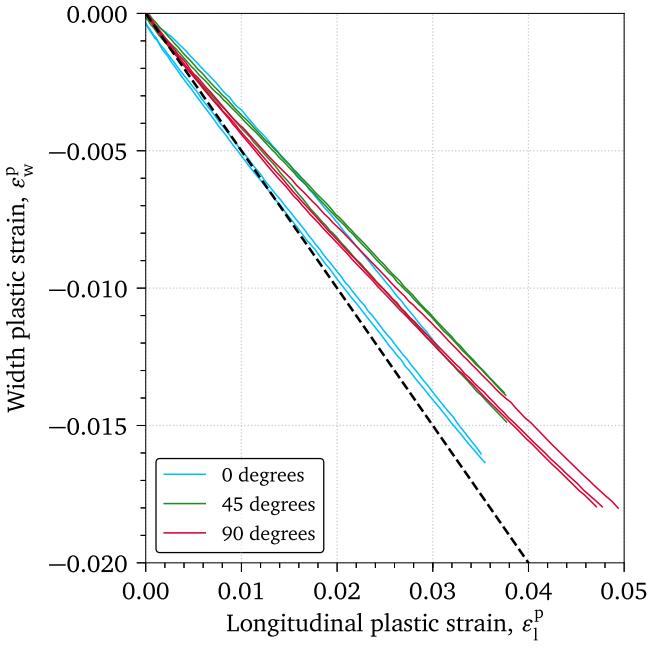

Fig. 9. Plastic strain paths during the tensile tests at the three different orientations measured from DIC data. The dashed line represents the theoretical path for isotropic plasticity.

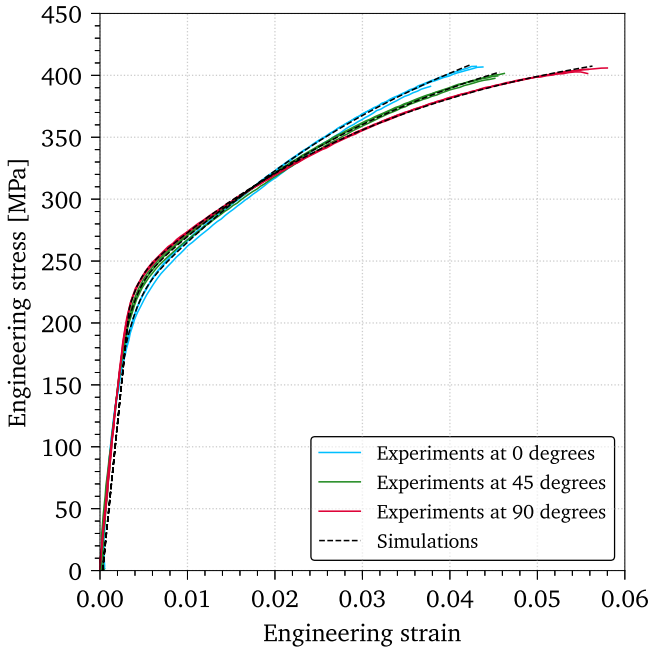

Fig. 10. Engineering stress–strain curves up to failure of the calibrated constitutive model and the experimental tests at 0, 45, and 90 degrees with respect to the printing direction.

with four and five elements through the thickness with insignificant differences compared to the model with three elements. Thus, this was assumed as a reasonable discretisation for a bending-governed problem, able to capture the curvature of the walls (Fyllingen et al., 2010). Taking advantage of the symmetry of the problem, only a quarter of the component was modelled and the pertinent boundary conditions

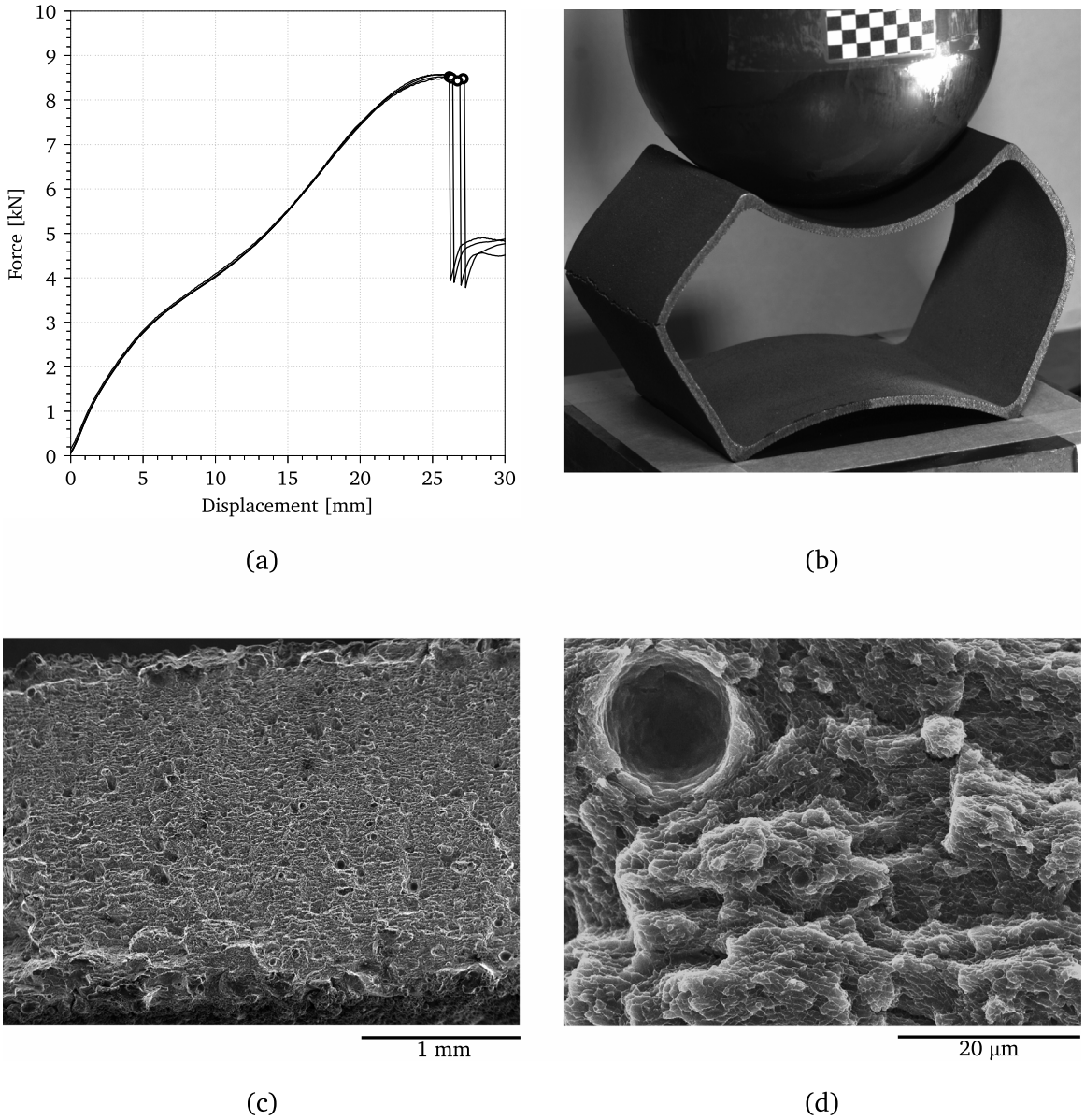

Fig. 11. Force–displacement curves of the four experimental lateral crushing tests (a), where the dots indicate the first failure, and picture of one of the tests after the first failure at the left wall (b). SEM images of the fracture surface at different scales, (c) and (d)

were applied at the faces coincident with the symmetry planes. The shell element model was meshed using an element size of 2.5 mm, equal to the nominal thickness of the component's walls. Since shell elements with a characteristic length smaller than their thickness can lead to unrealistic strain localisation, this element size was considered adequate even though the material presented a quasi-brittle behaviour and no localisation was observed in the tensile tests. The shell elements had five integration points through their thickness.

The spherical actuator and the reaction plate were modelled as infinitely rigid surfaces, and a friction coefficient of 0.05 was assumed in all contact interfaces. The generous lubrication of the surfaces in contact before each test justifies this relatively low friction coefficient. A time scaling factor of 3500 was used in all simulations, and quasi-static conditions were ensured with a smoothly-ramped velocity of the actuator and a check of the energy balance in every simulation.

In general, the finite element simulation results correlated well with the experimental tests (see Fig. 12). Both shell and solid models captured the global collapse and failure modes of the experiments (Figs. 12(b) and 12(d)), and a reasonably good agreement of the numerical and experimental force–displacement curves was achieved, as shown in Figs. 12(a) and 12(c). It is worth mentioning here that the reason for the removal of some elements from the mesh in Fig. 12(b) and not in Fig. 12(d) is due to the fact that Abaqus only removes an element when the damage variable D reaches a value of 1 at all its integration or section points. This happens in the solid elements – with only one integration point – but does not occur in the shells since not all their section points have failed. Even though the shell elements are not removed, the force drops due to the loss of load-carrying capacity of the elements when the outer integration point fails. A contour plot of the damage variable D is also displayed in Figs. 12(b) and 12(d), where the colour maps correspond to the visible face of the elements. Since the Cockcroft–Latham criterion does not accumulate any damage under compression, neither the inner wall faces nor the bottom part show any considerable damage.

As could be expected, the model with solid hexahedral elements predicted the critical force and displacement of the experimental tests with a higher degree of accuracy than that with shell elements. On the other hand, the shell elements offered a conservative result with an

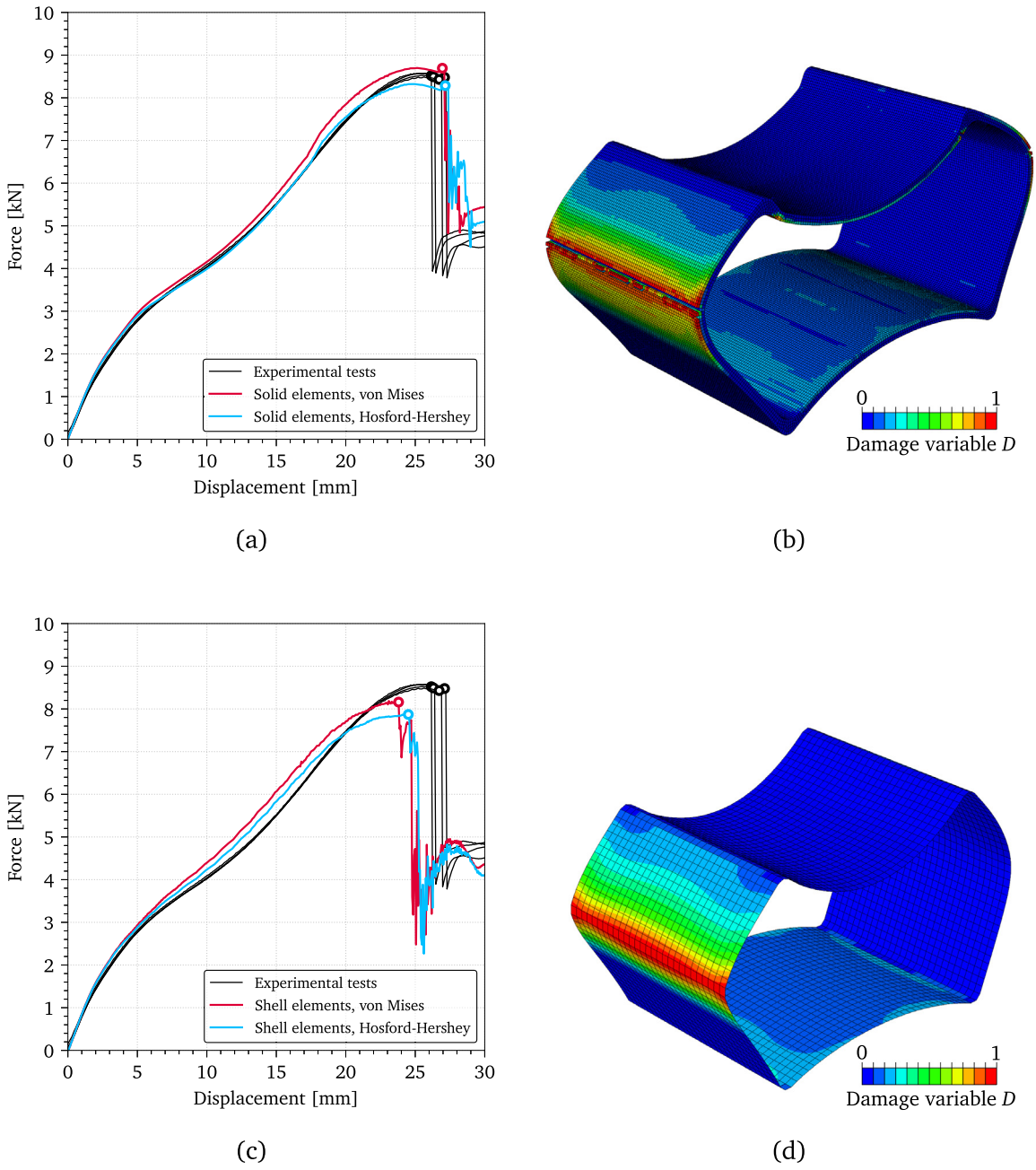

Fig. 12. Results of the simulations of the component tests: force–displacement curves with solid elements (a) and deformed shape at failure (b), and force–displacement curves with shells (c) and deformed shape at failure (d). Dots indicate failure.

acceptable accuracy and a computation time almost four times shorter than that of the solid element models.

4.3. Influence of the yield surface

Regarding the yield surfaces, the results were nearly identical in comparing the von Mises or the Hershey–Hosford criterion. The predicted forces were only 6% lower with the latter compared to the former in both the solid and shell finite element models. To further investigate the influence of the yield surface on the results, the stress state at the point where fracture initiates was analysed. The stress state can be characterised by the Lode parameter L and the stress triaxiality σ^*. The Lode parameter can be defined in terms of the principal stresses as

$$L = \frac{2\sigma_2 - \sigma_1 - \sigma_3}{\sigma_1 - \sigma_3}. \tag{10}$$

The Lode parameter L equals −1 in generalised tension, 0 in generalised shear and 1 in generalised compression. The stress triaxiality is defined as the ratio of the hydrostatic stress σ_H to the von Mises equivalent stress σ_{eq}, that is

$$\sigma^* = \frac{\sigma_H}{\sigma_{eq}}, \tag{11}$$

where the hydrostatic stress is defined as one third of the trace of the stress tensor, $\sigma_H = \frac{1}{3}\mathrm{tr}\,(\boldsymbol{\sigma})$.

Both the Lode parameter and the stress triaxiality were computed throughout the simulation at the fracture point of the side walls of the box, using the solid element model and the Hershey yield surface. The obtained results are provided in Fig. 13, and clearly depict a tensile-dominated scenario at fracture under plane strain conditions. Here, although the stress state in the component tests was different from that

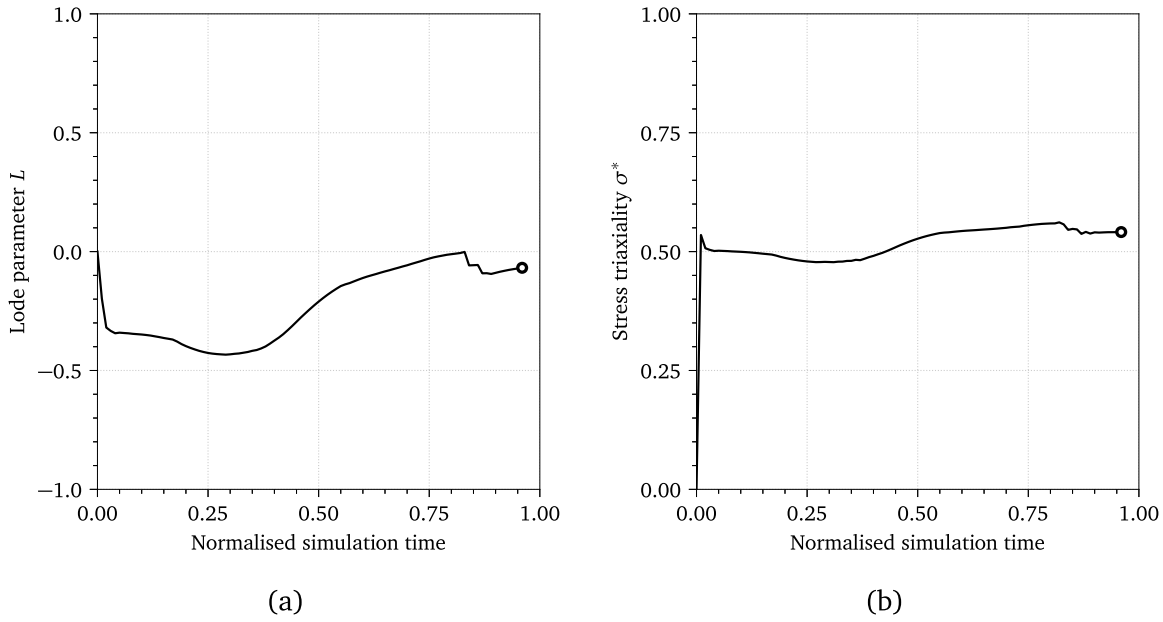

Fig. 13. Evolution of the Lode parameter (a) and the stress triaxiality (b) at a solid element located in the wall crack in the finite element model during the simulation. A dot indicates the failure point.

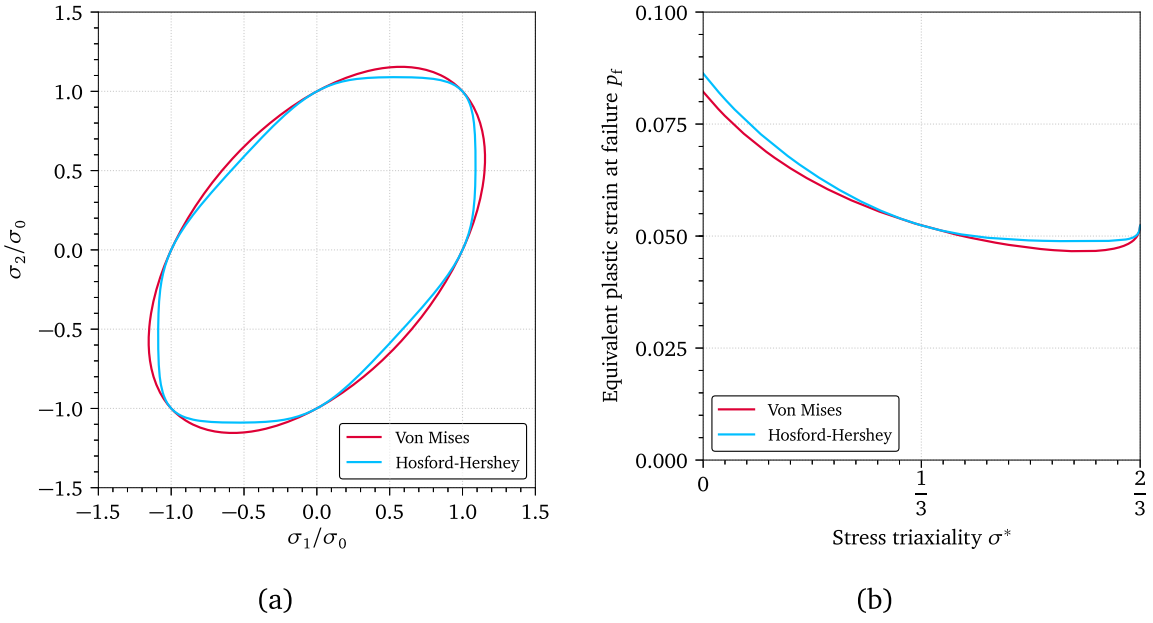

Fig. 14. Comparison of the von Mises and Hershey yield surfaces (a) and the fracture loci of the Cockroft–Latham criterion adopting one or another surface for the material calibrated at 90 degrees with the printing direction (b). Plane stress conditions are assumed in both figures.

in the uniaxial tension tests, the CL criterion was able to predict failure. This is in line with other works from the authors (Morin et al., 2017).

The Lode parameter takes values close to 0 at the point where the fracture of the component initiates, Fig. 13(a), which indicates a state of generalised shear. Under these conditions, the Hershey surface lies inside the von Mises surface, as shown in Fig. 14(a). This causes the material to yield earlier if the former criterion is adopted compared to the latter, which is translated into lower force levels in the simulations, see Figs. 12(a) and 12(c).

The force–displacement curves in Figs. 12(a) and 12(c) also show that the displacement at failure is somewhat larger with the Hershey–Hosford criterion than with the von Mises surface. The explanation behind this is the difference in fracture loci derived from the Cockcroft–Latham criterion if one or another yield criterion is adopted. These fracture loci for both yield surfaces are plotted in Fig. 14(b) for the material calibrated at 90 degrees with the printing direction and assuming plane stress conditions, where it can be seen that the Hershey criterion gives a higher ductility compared to the von Mises criterion under stress triaxialities around 0.5, like those observed in the simulations, Fig. 13(b). This increment in the failure strain is therefore translated into a larger displacement at failure in the component simulations when the Hershey–Hosford criterion is adopted.

4.4. Influence of the calibration direction in the results

Even though in the component tests the material was mainly loaded orthogonal to the printing direction, additional simulations were run

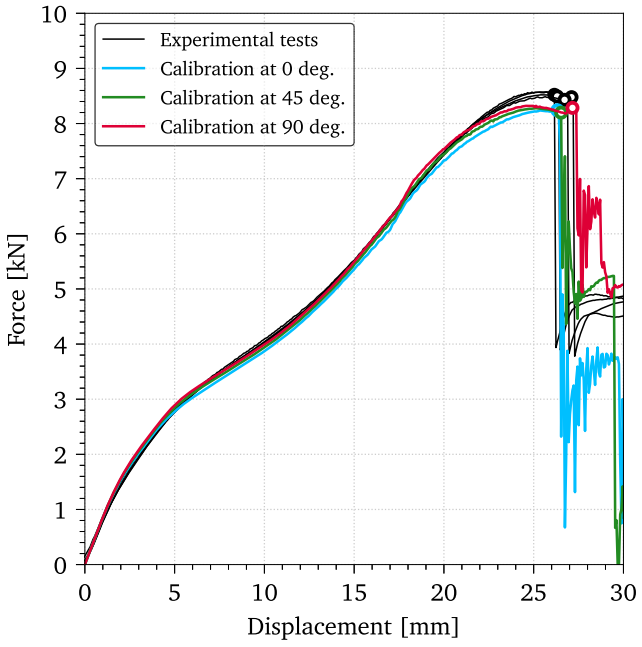

Fig. 15. Comparison of the force–displacement curves from the component tests and numerical simulations using different directions for the calibration of the constitutive model. Dots indicate failure.

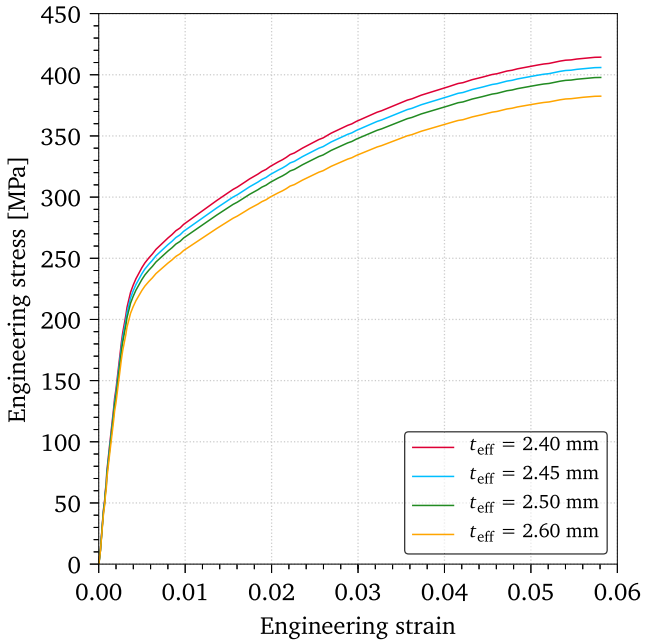

Fig. 16. Variation of the experimental engineering stress–strain curves for different effective thicknesses.

using the calibrated constitutive models for the other two tested directions with the parameters given in Table 2. This was done simplistically to assess how anisotropic work-hardening could affect the results. To this end, the solid elements model with the Hershey–Hosford yield criterion was employed. The results of these additional simulations are compared in Fig. 15, where it can be clearly seen that the differences between results obtained with different calibrations are very small. Although a different fracture strain was observed in the tensile tests in three directions (see Fig. 4), the variations in the initial yield stress and the work hardening balance this difference and keep the critical displacement in the component tests more or less unaltered regardless of the calibration direction.

4.5. Discussion on the effect of the effective thickness in the results

Given the superficial porosity of the as-printed AlSi10Mg alloy, it is not straightforward to determine an effective thickness for modelling and simulation purposes. In the present work, this t_{eff} has been estimated by averaging measurements taken on the microscope images of some material samples, which resulted on the effective thickness being 2% lower than the nominal thickness. This strategy – however effective for this case – is not necessarily the best or most practical, and the obtained value is not free of uncertainty.

In order to see how far the choice of one or another value for the thickness would affect the results, a short parametric study was conducted. This required not only changing the thickness in the component models, but also re-calibrating the material constitutive model and the fracture parameter for each case, since the experimental engineering stress–strain curves vary depending on the assumed thickness. To that end, additional calibrations were conducted for effective thicknesses t_{eff} of 2.40, 2.50 (nominal), and 2.60 mm, resulting in the stress–strain curves plotted in Fig. 16 for a representative test at 90 degrees with the printing direction. As could be expected, the work hardening remained more or less the same for all t_{eff}, whereas the initial yield stress gradually decreased as the effective thickness increased, from 219 MPa for t_{eff} = 2.40 mm to 199 MPa for t_{eff} = 2.60 mm.

The component simulations were then re-run with these additional effective thicknesses and material properties using Hershey's yield surface exclusively, for the sake of brevity. Three elements across the thickness were enforced in the solid elements model in all simulations, whereas the element size of the shells was kept constant at 2.5 mm. The force–displacement curves obtained from these simulations are provided in Fig. 17, together with the curves for the effective thickness of 2.45 mm. Whereas all the curves follow the same trend, a certain influence of the effective thickness on the force and displacement at failure is noticed. The reason for the more irregular trend of this critical point in Fig. 17(a) was failure being initiated at the corners of the top part of the box instead of the side walls for thicknesses of 2.40 and 2.60 mm. In the experimental tests it was observed that failure initiated always in the side walls, and so happened in the simulations with thicknesses of 2.45 and 2.50 mm.

In light of these results, it seems that a correct determination of the effective thickness is significant for an accurate simulation of 3D-printed metal parts. In view of Figs. 12, 15 and 17, the effective thickness has more impact on the results than the anisotropic work-hardening and the curvature of the yield surface.

5. Conclusions

Finite element simulations of additively manufactured metal boxes in AlSi10Mg under lateral crushing were conducted and compared to experimental results. The material constitutive models were supported by an adequate experimental campaign. The following conclusions can be drawn from the present study:

- The as-built AlSi10Mg was proved slightly anisotropic in stresses, but more strongly anisotropic regarding the plastic flow. The fracture strain showed also some anisotropy. A good repeatability of both material and component tests was observed too.
- The behaviour of the 3D-printed boxes under lateral crushing was correctly captured by the same modelling and simulation strategies commonly used for rolled or extruded aluminium alloys, using a purely isotropic constitutive model and an isotropic failure criterion. Two different isotropic yield surfaces were employed with no great difference in the results. Therefore, these

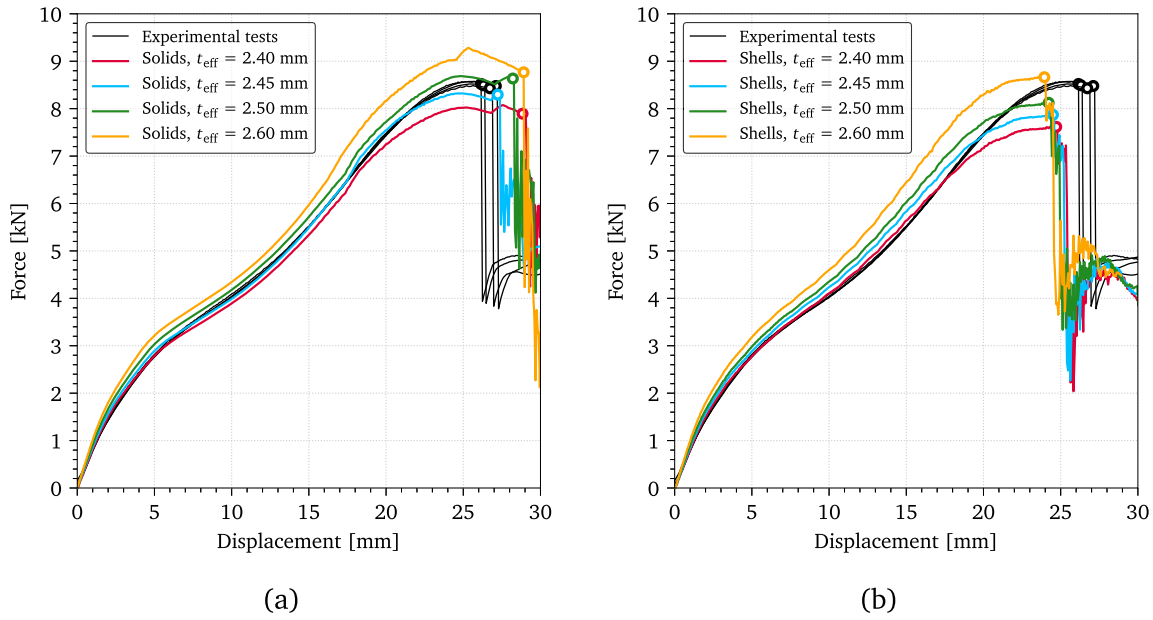

Fig. 17. Influence of the effective thickness t_{eff} on the force–displacement curves of the component tests simulated with solid elements (a) and shell elements (b).

common modelling strategies seem well suited for the simulation of parts manufactured by selective laser melting under large deformations and fracture.

- The choice of one or another direction for calibrating the constitutive model of the material showed no remarkable effects in the results of the component simulations.
- A microscopy analysis showed that the as-printed material exhibited a high porosity, stemming from the printing process. From a mechanical point of view, this porosity might have induced the quasi-brittle failure of the material.
- Related to the previous conclusion, the elevated roughness of the as-built AlSi10Mg presented challenges in adopting an effective thickness for the finite element modelling. It was shown that the determination of this effective thickness based on microscopy images offered good results compared to other values in a parametric study. For this material, effective thickness was 2% lower than the nominal thickness.
- The results of the simulations were notably sensitive to the adopted effective thickness. Thus, a correct determination of this parameter is important.

Declaration of competing interest

The authors declare that they have no known competing financial interests or personal relationships that could have appeared to influence the work reported in this paper.

Acknowledgements

The authors would like to acknowledge the financial support from the Centre for Advanced Structural Analysis, SFI-CASA (Project No. 237885), funded by the Research Council of Norway and NTNU. Microscopy, metallographic and SEM studies were carried out by Laboratory of Optical Metallography at CENIM-CSIC, and National Centre of Electron Microscopy (ICTS-CNME UCM) in Madrid, Spain. The 3D-printed parts were manufactured by Tronrud Engineering in Hønefoss (Norway). All the laboratory work was carried out with help from Mr. Tore Wisth and Mr. Trond Auestad. Thanks also to Ms. Maisie Edwards-Mowforth for improving the English language.

References

Aboulkhair, N.T., Everitt, N.M., I.A., Tuck, C., 2014. Reducing porosity in AlSi10Mg parts processed by selective laser melting. Addit. Manuf. 1–4, 77–86.

Andani, M.T., Karamooz-Ravari, M.R., Mirzaeifar, R., Ni, J., 2018. Micromechanics modeling of metallic alloys 3D printed by selective laser melting. Mater. Des. 137, 204–213.

Anon, 2016. ABAQUS 2017 Documentation. Dassault Systèmes, Providence Road, Rhode Island.

Anon, 2018. User manual - ecorr - digital image correlation tool. https://www.ntnu.edu/kt/ecorr. (Accessed 03 May 2018).

Barlat, F., Aretz, H., Yoon, J.W., Karabin, M.E., Brem, J.C., Dick, R.E., 2005. Linear transfomation-based anisotropic yield functions. Int. J. Plast. 21 (5), 1009–1039.

Beevers, E., Brandão, A.D., Gumpinger, J., Gschweitl, M., Seyfert, C., Hofbauer, P., Rohr, T., Ghidini, T., 2018. Fatigue properties and material characteristics of additively manufactured AlSi10Mg – Effect of the contour parameter on the microstructure, density, residual stress, roughness and mechanical properties. Int. J. Fatigue 117, 148–162.

Bonatti, C., Mohr, D., 2019. Mechanical performance of additively-manufactured anisotropic and isotropic smooth shell-lattice materials: Simulations & experiments. J. Mech. Phys. Solids 122, 1–26.

Boschetto, A., Bottini, L., Veniali, F., 2017. Roughness modeling of AlSi10Mg parts fabricated by selective laser melting. J. Mater Process. Technol. 241, 154–163.

Cockcroft, M.G., Latham, D.J., 1968. Ductility and the workability of metals. Journal of the Institute of Metals 96, 33–39.

Costas, M., Morin, D., Hopperstad, O.S., Børvik, T., Langseth, M., 2019. A through-thickness damage regularisation scheme for shell elements subjected to severe bending and membrane deformations. J. Mech. Phys. Solids 123, 190–206.

Dæhli, L.E.B., Morin, D., Børvik, T., Hopperstad, O.S., 2017. Influence of yield surface curvature on the macroscopic yielding and ductile failure of isotropic porous plastic materials. J. Mech. Phys. Solids 107, 253–283.

Delahaye, J., Tchoufang Tchuindjang, J., Lecomte-Beckers, J., Rigo, O., Habraken, A.M., Mertens, A., 2019. Influence of Si precipitates on fracture mechanisms of AlSi10Mg parts processed by Selective Laser Melting. Acta Mater. 175, 160–170.

Domfang Ngnekou, J.N., Nadot, Y., Henaff, G., Nicolai, J., Kan, W.H., Cairney, J.M., Ridosz, L., 2019. Fatigue properties of AlSi10Mg produced by additive layer manufacturing. Int. J. Fatigue 119, 160–172.

Fagerholt, E., Børvik, T., Hopperstad, O.S., 2013. Measuring discontinuous displacement fields in cracked specimens using digital image correlation with mesh adaptation and crack-path optimization. Opt. Lasers Eng. 51 (3), 299–310.

Fyllingen, Ø., Hopperstad, O.S., Hanssen, A.G., Langseth, M., 2010. Modelling of tubes subjected to axial crushing. Thin-Walled Struct. 48 (2), 134–142.

Girelli, L., Giovagnoli, M., Tocci, M., Pola, A., Fortini, A., Merlin, M., Marina La Vecchia, G., 2019b. Evaluation of the impact behaviour of AlSi10Mg alloy produced using laser additive manufacturing. Mater. Sci. Eng. A 748, 38–51.

Girelli, L., Tocci, M., Gelfi, M., Pola, A., 2019a. Study of heat treatment parameters for additively manufactured AlSi10Mg in comparison with corresponding cast alloy. Mater. Sci. Eng. A 739, 317–328.

Khadyko, M., Marioara, C.D., Dumoulin, S., Børvik, T., Hopperstad, O.S., 2017. Effects of heat-treatment on the plastic anisotropy of extruded aluminium alloy AA6063. Mater. Sci. Eng. A 708, 208–221.

Kim, D.-K., Hwang, J.-H., Kim, E.-Y., Heo, Y.-U., Woo, W., Choi, S.-H., 2017. Evaluation of the stress–strain relationship of constituent phases in AlSi10Mg alloy produced by selective laser melting using crystal plasticity FEM. J. Alloys Compd. 714, 687–697.

Kristoffersen, M., Costas, M., Koenis, T., Brøtan, V., Paulsen, C.O., Børvik, T., 2020. On the ballistic perforation resistance of additive manufactured AlSi10Mg aluminium plates. Int. J. Impact Eng. 137, 103476.

Kruth, J.-P., Levy, G., Klocke, F., Childs, T.H.C., 2007. Consolidation phenomena in laser and powder-bed based layered manufacturing. CIRP Ann. 56 (2), 730–759.

Kruth, J.-P., Mercelis, P., Van Vaerenbergh, J., Froyen, L., Rombouts, M., 2005. Binding mechanisms in selective laser sintering and selective laser melting. Rapid Prototyp. J. 11 (1), 26–36.

Larrosa, N.O., Wang, W., Read, N., Loretto, M.H., Evans, C., Carr, J., Tradowsky, U., Attallah, M.M., Withers, P.J., 2018. Linking microstructure and processing defects to mechanical properties of selectively laser melted AlSi10Mg alloy. Theor. Appl. Fract. Mech. 98, 123–133.

Lemaitre, J., Desmorat, R., 2005. Engineering Damage Mechanics: Ductile, Creep, Fatigue and Brittle Failures. Springer Berlin Heidelberg.

Morin, D., Kaarstad, B.L., Skajaa, B., Hopperstad, O.S., Langseth, M., 2017. Testing and modelling of stiffened aluminium panels subjected to quasi-static and low-velocity impact loading. Int. J. Impact Eng. 110, 97–111.

Müller, J.R., Panarotto, M., Malmqvist, J., Isaksson, O., 2018. Lifecycle design and management of additive manufacturing technologies. Proc. Manuf. 19, 135–142.

Saai, A., Dumoulin, S., Hopperstad, O.S., Lademo, O.-G., 2013. Simulation of yield surfaces for aluminium sheets with rolling and recrystallization textures. Comput. Mater. Sci. 67, 424–433.

Scherillo, F., 2018. Chemical surface finishing of AlSi10Mg components made by additive manufacturing. Manuf. Lett.

Tancogne-Dejean, T., Spierings, A.B., Mohr, D., 2016. Additively-manufactured metallic micro-lattice materials for high specific energy absorption under static and dynamic loading. Acta Mater. 116, 14–28.

Tang, M., Pistorius, P.C., 2017. Oxides, porosity and fatigue performance of AlSi10Mg parts produced by selective laser melting. Int. J. Fatigue 94, 192–201.

Trevisan, F., Calignano, F., Lorusso, M., Jukka, P., Aversa, A., Ambrosio, E.P., Lombardi, M., Fino, P., Manfredi, D., 2017. On the selective laser melting (SLM) of the AlSi10Mg alloy: Process, microstructure, and mechanical properties. Materials 10 (1).

Wadley, H.N.G., Børvik, T., Olovsson, L., Wetzel, J.J., Dharmasena, K.P., Hopperstad, O.S., Deshpande, V.S., Hutchinson, J.W., 2013. Deformation and fracture of impulsively loaded sandwich panels. J. Mech. Phys. Solids 61 (2), 674–699.

Weingarten, C., Buchbinder, D., Pirch, N., Meiners, W., Wissenbach, K., Poprawe, R., 2015. Formation and reduction of hydrogen porosity during selective laser melting of AlSi10Mg. J. Mater Process. Technol. 221, 112–120.

Xiong, Z.H., Liu, S.L., Li, S.F., Shi, Y., Yang, Y.F., Misra, R.D.K., 2019. Role of melt pool boundary condition in determining the mechanical properties of selective laser melting AlSi10Mg alloy. Mater. Sci. Eng. A 740–741, 148–156.

Yang, K., Xu, S., Zhou, S., Shen, J., Xie, Y.M., 2017a. Design of dimpled tubular structures for energy absorption. Thin-Walled Struct. 112, 31–40.

Yang, Z., Yu, Y., Wei, Y., Huang, C., 2017b. Crushing behavior of a thin-walled circular tube with internal gradient grooves fabricated by SLM 3D printing. Thin-Walled Struct. 111, 1–8.

Yu, W., Sing, S.L., Chua, C.K., Tian, X., 2019. Influence of re-melting on surface roughness and porosity of AlSi10Mg parts fabricated by selective laser melting. J. Alloys Compd. 792, 574–581.

Zhang, Y., Liu, T., Ren, H., Maskery, I., Ashcroft, I., 2018. Dynamic compressive response of additively manufactured AlSi10Mg alloy hierarchical honeycomb structures. Compos. Struct. 195, 45–59.

Zhou, L., Mehta, A., Schulz, E., McWilliams, B., Cho, K., Sohn, Y., 2018. Microstructure, precipitates and hardness of selectively laser melted AlSi10Mg alloy before and after heat treatment. Mater. Charact. 143, 5–17.